NANO LETTERS

pubs.acs.org/NanoLett Letter

Plasmon-Enhanced Expansion Microscopy

Priya Rathi, Prashant Gupta, Avishek Debnath, Harsh Baldi, Yixuan Wang, Rohit Gupta, Baranidharan Raman,* and Srikanth Singamaneni*

Cite This: *Nano Lett.* 2023, 23, 5654−5662 Read Online

ACCESS | Metrics & More | Article Recommendations | Supporting Information

ABSTRACT: Expansion microscopy (ExM) is a rapidly emerging super-resolution microscopy technique that involves isotropic expansion of biological samples to improve spatial resolution. However, fluorescence signal dilution due to volumetric expansion is a hindrance to the widespread application of ExM. Here, we introduce plasmon-enhanced expansion microscopy (p-ExM) by harnessing an ultrabright fluorescent nanoconstruct, called plasmonic-fluor (PF), as a nanolabel. The unique structure of PFs renders nearly 15000-fold brighter fluorescence signal intensity and higher fluorescence retention following the ExM protocol (nearly 76%) compared to their conventional counterparts (<16% for IR-650). Individual PFs can be easily imaged using conventional fluorescence microscopes, making them excellent "digital" labels for ExM. We demonstrate that p-ExM enables improved tracing and decrypting of neural networks labeled with PFs, as evidenced by improved quantification of morphological markers (nearly a 2.5-fold increase in number of neurite terminal points). Overall, p-ExM complements the existing ExM techniques for probing structure−function relationships of various biological systems.

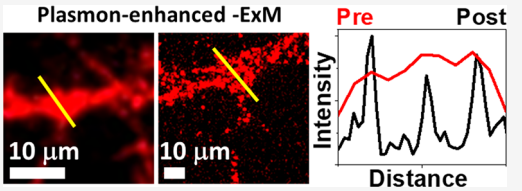

KEYWORDS: *expansion microscopy, fluorescence microscopy, plasmon-enhanced fluorescence, nanoneuro interaction, plasmonic-fluor*

Understanding the structure and structure−function relationships at various length scales is of paramount importance in various fields of biology and the life sciences. Optical microscopy is one of the most commonly used techniques to probe the structure and function of biological systems. The resolution of conventional optical microscopes, largely governed by the wavelength of the light, the refractive index of the surrounding medium, and the numerical aperture of the lens, is often limited to ∼250 nm.[1,2] Electron microscopes, on the other hand, can achieve a spatial resolution of a few angstroms, which enables the visualization of ultrafine structural details of cellular and subcellular structures.[3] However, the sample preparation for electron microscopy is complex, involving fixation to stabilize the sample under a high vacuum, microtoming to achieve thin sections for electron penetration, and staining for better visualization. Additionally, electron microscopy imaging often involves long imaging and analysis times, resulting in low throughput, and can be very expensive.

Advances in optical microscope technology, detection methods, and novel computational methodologies led to the advent of super-resolution microscopy techniques such as stimulated emission depletion (STED) microscopy, stochastic optical reconstruction microscopy (STORM), and minimal photon fluxes (MINFLUX), which allow spatial resolution below the diffraction limit of light.[4−6] For example, STED microscopy works by reducing the excitation volume, which minimizes the area generating fluorescence. This is done by using a donut-shaped laser beam that selectively quenches the fluorescence from surrounding regions through stimulated emission depletion.[4,5,7] Therefore, only molecules at the center of the excitation area will emit light, resulting in a higher-resolution image, overcoming diffraction limitation. STORM involves stochastically turning on specific fluorescent molecules within the diffraction-limited volume at specific time points, therefore unraveling the molecular localization over time and generating a super-resolution image.[8,9] MINFLUX combines fundamental approaches from STED and STORM, enabling high precision and high-resolution imaging.[10,11] These powerful imaging tools overcome the optical diffraction limit with a spatial resolution of ∼20−120 nm.[6,12] However, limited availability of these tools (often in centralized facilities), low throughput, and longer imaging and analysis time scales hinder their widespread and routine use.

Expansion microscopy (ExM) is a super-resolution technique compatible with existing optical microscopes that has received wide attention, since its introduction in 2015.[13,14] ExM is based on the physical expansion of fluorophore-labeled biological specimens anchored to a swellable polymer gel, enabling ∼70 nm lateral resolution.[13,14] The simple, inexpensive, and accessible nature of ExM has allowed biology and biomedical researchers to rapidly adopt this method and

Received: April 7, 2023
Revised: June 5, 2023
Published: June 12, 2023

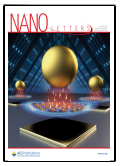

https://doi.org/10.1021/acs.nanolett.3c01256
Nano Lett. 2023, 23, 5654−5662

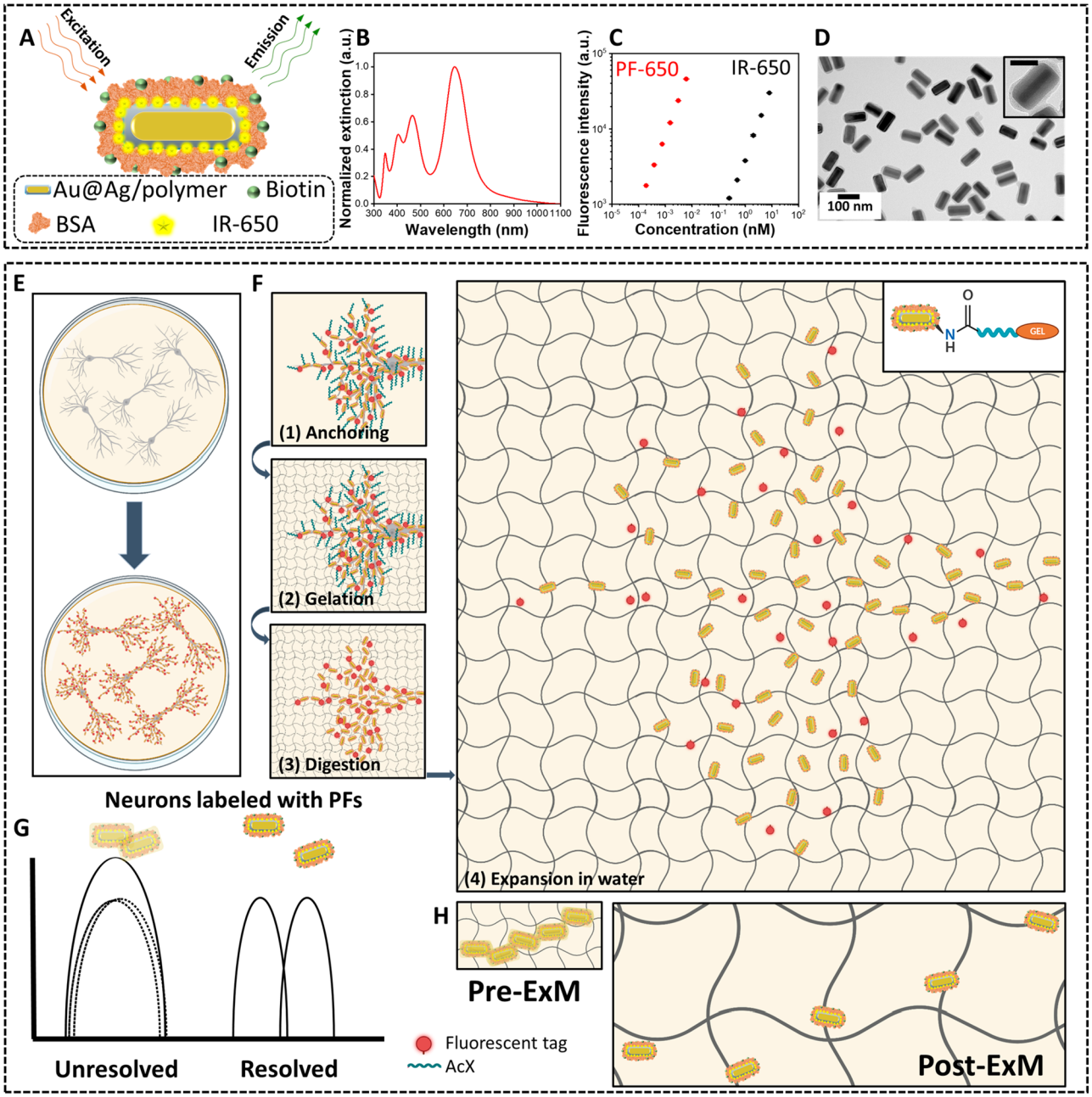

Figure 1. Plasmon-enhanced expansion microscopy (p-ExM). (A) Schematic illustration of PF-650 composed of a plasmonic nanostructure (Au@Ag nanocuboid), spacer layer (gray region), conjugated fluorescent dye molecules (IR-650), and a layer of BSA-biotin conjugate. (B) Visible−NIR spectra of PF-650. (C) Fluorescence intensity of PF-650 showing nearly 15000-fold increase in fluorescence intensity compared to IR-650. Error bars represent sd (n = 3 independent tests). (D) TEM image of PF-650 with inset image (scale bar 50 nm) showing the core nanostructure and outer shell comprised of a polymer spacer and BSA-biotin, (E) Schematic illustration to demonstrate the specific and spontaneous passive binding of negatively charged PFs to neurons. (F) Neurons labeled with PFs are fixed, immunostained, and subjected to standard expansion microscopy protocol steps: (1) anchoring Acryloyl-X to serve as a link between biomolecules and gel, (2) gelation step resulting in the formation of a hydrogel, (3) digestion step resulting in the breakdown of nonanchored cellular structure while retaining the anchored biomolecules including PFs, (4) expansion of gel when exposed to water resulting in ∼4× expansion. (G) Schematic showing physical separation and improved spatial resolution of clustered PFs upon sample expansion. (H) Enlarged region depicting closely located PFs in the gel matrix that remains unresolved (left) until subjected to water, resulting in the creation of physical space between PFs, allowing enhanced resolution.

develop modified versions for their specific needs.[15−17] ExM relying on conventional molecular fluorophores suffers from significant degradation in fluorescence intensity (>50%) following the expansion process owing to (i) degradation of fluorescent dye when treated with proteinase K during the digestion step in ExM protocol; and (ii) the physical expansion as a result of ExM, which results in the dilution of the fluorescence signal.[14,18,19] This reduction in the volumetric density of fluorophores significantly diminishes the quantitative and qualitative applications of ExM. In addition, commonly used fluorophores such as Alexa Fluor 647 and Cy5 are known to be completely damaged during the ExM process, precluding their use in ExM.[13,14] These considerations highlight the need for ultrabright fluorescent labels in ExM that

https://doi.org/10.1021/acs.nanolett.3c01256
Nano Lett. 2023, 23, 5654−5662

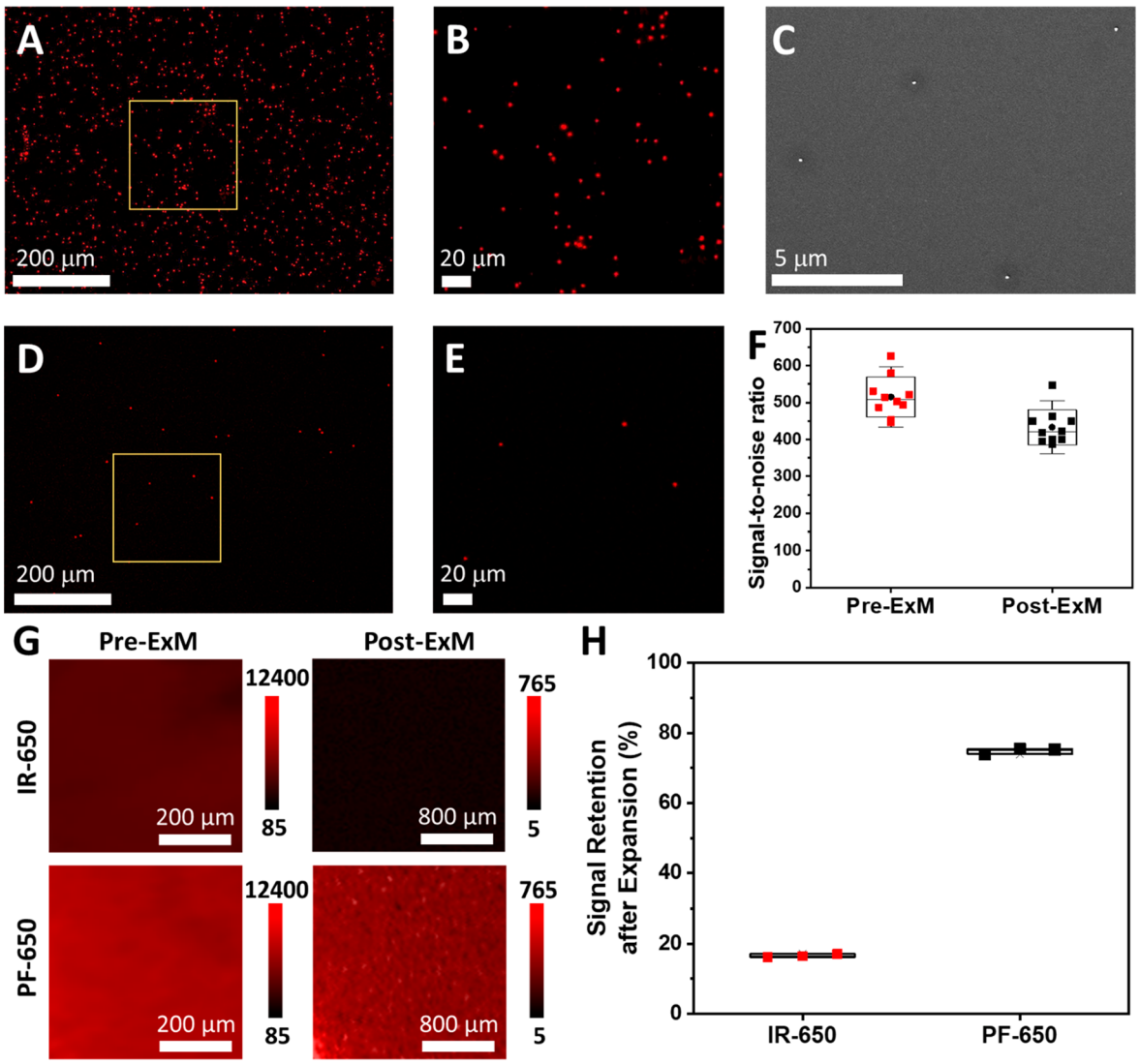

Figure 2. Stability of plasmonic-fluors in expansion microscopy. (A) Confocal 10× fluorescence image of PF-650 immobilized on a BSA-biotinylated glass coverslip under pre-ExM conditions. (B) Enlarged confocal fluorescence image showing the sparsely adsorbed PF-650, with occasional occurrences of PFs in close proximity. (C) Scanning electron microscopy imaging of PF-650 from (A) showing well-dispersed PF-650, highlighting the better resolving power of electron microscopy over light microscopy. (D) Confocal 10× fluorescence image of PF-650 immobilized on a BSA-biotinylated glass coverslip under post-ExM conditions. (E) Enlarged confocal fluorescence image highlighting the large physical separation created between individual PF-650 plasmonic-fluors, allowing them to be resolved and counted as digital nanolabels. (F) Signal-to-noise ratio (SNR) corresponding to PF-650 under pre-ExM and post-ExM conditions, exhibiting nearly 85% fluorescence retention under post-ExM conditions. (G) Fluorescence images of IR-650 dye and PF-650 immobilized on a biotinylated BSA-coated glass coverslip under pre-ExM and post-ExM conditions ,highlighting better signal retention of PF-650 after expansion compared to IR-650 dye. (Note: color scale bars under post-ExM conditions were set to be 16-fold lower compared to pre-ExM conditions in order to account for the 16-fold signal dilution associated with the expansion.) (H) Corresponding percentage signal retentions of PF-650 and IR-650 dye after expansion.

can mitigate the signal dilution challenges and promote a more widespread adoption of the technology.

Here, for the first time, we demonstrate plasmon-enhanced expansion microscopy (p-ExM) by harnessing an ultrabright, fluorescent nanolabel called plasmonic-fluor (PF). We investigate the compatibility of PFs with ExM and the stability of individual PFs against signal dilution after sample expansion. We also show the high fidelity and isotropic expansion of a sample comprised of hippocampal neurons labeled with PFs. p-ExM enabled improved spatial resolution and more accurate quantification of morphological parameters of the neuronal network compared with conventional confocal fluorescence microscopy. p-ExM complements conventional ExM (relying on molecular fluorophores) in overcoming the challenges associated with signal dilution and imaging of low-abundance cell surface markers.

We have recently introduced an ultrabright nanoconstruct termed a plasmonic-fluor that exhibits a more than 3 orders of magnitude brighter fluorescence signal compared to its conventional counterpart.[20] Plasmonic-fluor is composed of a plasmonic nanostructure as a fluorescence enhancer, molecular fluorophores as light emitters, a polymer spacer layer to avoid metal-induced quenching of the fluorescence, bovine serum albumin (BSA) on the surface to minimize nonspecific binding in bioassays, and a universal biolinker (e.g., biotin, streptavidin) (Figure 1A). We have demonstrated that plasmonic-fluors can replace conventional molecular fluorophores in various bioassays to enable nearly 1000-fold

https://doi.org/10.1021/acs.nanolett.3c01256
Nano Lett. 2023, 23, 5654−5662

improvement in the limit of detection without significantly changing the workflow or read-out devices.[20−23] Plasmonic-fluors can be realized with any molecular fluorophore of choice by tuning the localized surface plasmon resonance (LSPR) wavelength of the plasmonic nanostructure to match the excitation/emission wavelength of the fluorophore.[20,22] As such, plasmonic-fluors can be designed and synthesized to emit over a broad range of electromagnetic wavelengths.

In this study, we harnessed negatively charged plasmonic-fluors comprised of IR-650 (called PF-650 henceforth) to demonstrate plasmon-enhanced expansion microscopy.[24] It has been previously reported that negatively charged nanostructures, irrespective of their size, shape, and composition, specifically bind to neurons.[25] Plasmonic-fluor-650 is realized using Au@Ag nanocuboids with an LSPR wavelength at ∼650 nm as a plasmonic nanoantenna (Figure 1B). The resulting PFs are negatively charged with a ζ potential of −28 ± 3 mV, owing to the presence of BSA on the outer surface. Transmission electron microscopy (TEM) images show PF-650 with a length of 110 ± 7 nm and a width of 45 ± 3 nm (Figure 1D).

Briefly, expansion microscopy (ExM) protocol comprises labeling biological specimens and anchoring them to a swellable polyelectrolyte gel, which when exposed to water undergoes uniform physical expansion, resulting in a physical separation between labeled biomolecules.[13,14] We harnessed the specific interactions between the negatively charged PFs and hippocampal neurons to realize plasmon-enhanced expansion microscopy (Figure 1E). A neuronal culture labeled with PFs, immunostained, and fixed is introduced to an anchoring molecule (Acryloyl-X) in the first step of ExM (Figure 1F). The anchor covalently binds with the tagged biomolecules and PFs. Subsequently, the PF-labeled neurons are exposed to a swellable polyelectrolyte gel precursor solution comprised of monomer precursors (sodium acrylate, acrylamide), cross-linker (*N*,*N*′-methylenebis(acrylamide)), free-radical initiator (ammonium persulfate), and accelerator (tetramethylethylenediamine), resulting in the formation of a cross-linked polymer network.[13,15] Next, the polymer network−sample composite is subjected to proteinase K solution that cleaves nonanchored regions in the PF-labeled neuron sample to ensure isotropic expansion and homogenization. Finally, the homogenized polymer network sample is immersed in water, resulting in swelling and isotropic physical expansion of the PF-hydrogel.

Conventional molecular fluorophores such as DyLight 405, AF546, and CF633 and fluorescent proteins such as GFP exhibit ∼50% loss of fluorescence after being subjected to the ExM protocol.[13,14,18] In some cases such as AF647 and Cy5, proteinase K digestion causes severe degradation of the fluorophores, forbidding their use in ExM.[14] Hence, it is important to probe the compatibility of PFs with the ExM protocol. To quantify the fluorescence retention of PFs following the ExM protocol, PF-650 molecules were sparsely immobilized on glass coverslips using biotin−streptavidin interaction (see Materials and Methods in the Supporting Information). Confocal fluorescence microscopy images revealed bright fluorescence signals from sparsely adsorbed individual PF-650 molecules (Figure 2A,B). Scanning electron microscopy imaging confirmed the uniform and sparse distribution of individual PF-650 molecules on the surface (Figure 2C). Glass coverslip substrates with such a sparse distribution of PFs were subsequently subjected to a standard expansion protocol and imaged using a confocal microscope (Figure 2D,E). We quantified the fluorescence signal retention by comparing the signal-to-noise ratio (SNR) under pre-ExM and post-ExM conditions. The SNR for PF-650 was found to be 515 ± 52 under pre-ExM and 433 ± 45 under post-ExM conditions (Figure 2F). The post-ExM fluorescence intensity amounts to nearly 85% retention in fluorescence signal, which confirms the applicability of PF-650 as labels in ExM. Accordingly, to further validate the advantage of employing PFs in ExM over conventional molecular fluorophores, we compared the signal retentions of PF-650 and IR-650 (molecular fluorophore employed in the synthesis of PF-650) post-expansion over a large area, analogous to the real samples. We employed a biotin−streptavidin interaction to achieve circular spots (∼2 mm in diameter, n = 3) of PF-650 or IR-650 (Figure 2G). To achieve a quantifiable fluorescence intensity for IR-650 and avoid signal saturation of PF-650, we have used a nearly 4000-fold higher concentration of IR-650 compared to PF-650 (see the Supporting Information for details). The relatively small (∼10-fold) difference in the intensities between PF-650 and IR-650 is due to the vastly different concentrations of the two labels used in this experiment. We measured the mean fluorescence intensity (MFI) of these spots pre- and post-ExM and the signal retention was calculated as

$$\text{signal retention (\%)} = \frac{16 \times \text{MFI}_{\text{Post}}}{\text{MFI}_{\text{Pre}}} \times 100$$

where MFI_{Post} and MFI_{Pre} refers to mean fluorescence intensity post- and pre-ExM. Considering the 4-fold expansion of the sample and taking the resulting signal dilution into account, MFI_{Post} was multiplied by a factor of 16 in calculating the signal retention. We found that the signal retention with PF-650 post-ExM was ∼76% while the signal retention for its molecular counterpart (IR-650) was less than 16% (Figure 2H). The 76% signal retention measured using these relatively large samples is consistent with the 85% signal retention observed for individual PFs as described above. The high fluorescence signal retention of PFs can be ascribed to the unique design of the fluorescent nanoconstruct, in which the molecular fluorophores are protected against the harsh conditions during gelation and swelling. The molecular fluorophores are protected by the BSA coating on the surface of the plasmonic-fluors, thus shielding them from the (bio)chemical degradation during the sample expansion process.

Following the sample expansion, as expected, we noted a larger physical separation between the PFs immobilized on the glass coverslip. It is worth noting that the fluorescence signal from PFs is not spatially diffused after the ExM process as the molecular fluorophores are conjugated to the polymer spacer on the plasmonic core and remain intact after the ExM process. PFs serve as "digital nanolabels" allowing digitization of the fluorescence signal from individual PFs.[21] Overall, the excellent stability of the fluorescence signal and localization of the fluorescence signal of PFs after ExM make them attractive nanolabels for ExM.

Since its introduction in 2015, ExM has been extensively explored for imaging various features of neurons, including dendrites, dendritic spines, axons, and synaptic connections.[13,19,26] Expanding the sample and imaging the fluorescently labeled dendritic spines have been shown to provide

https://doi.org/10.1021/acs.nanolett.3c01256
Nano Lett. 2023, 23, 5654−5662

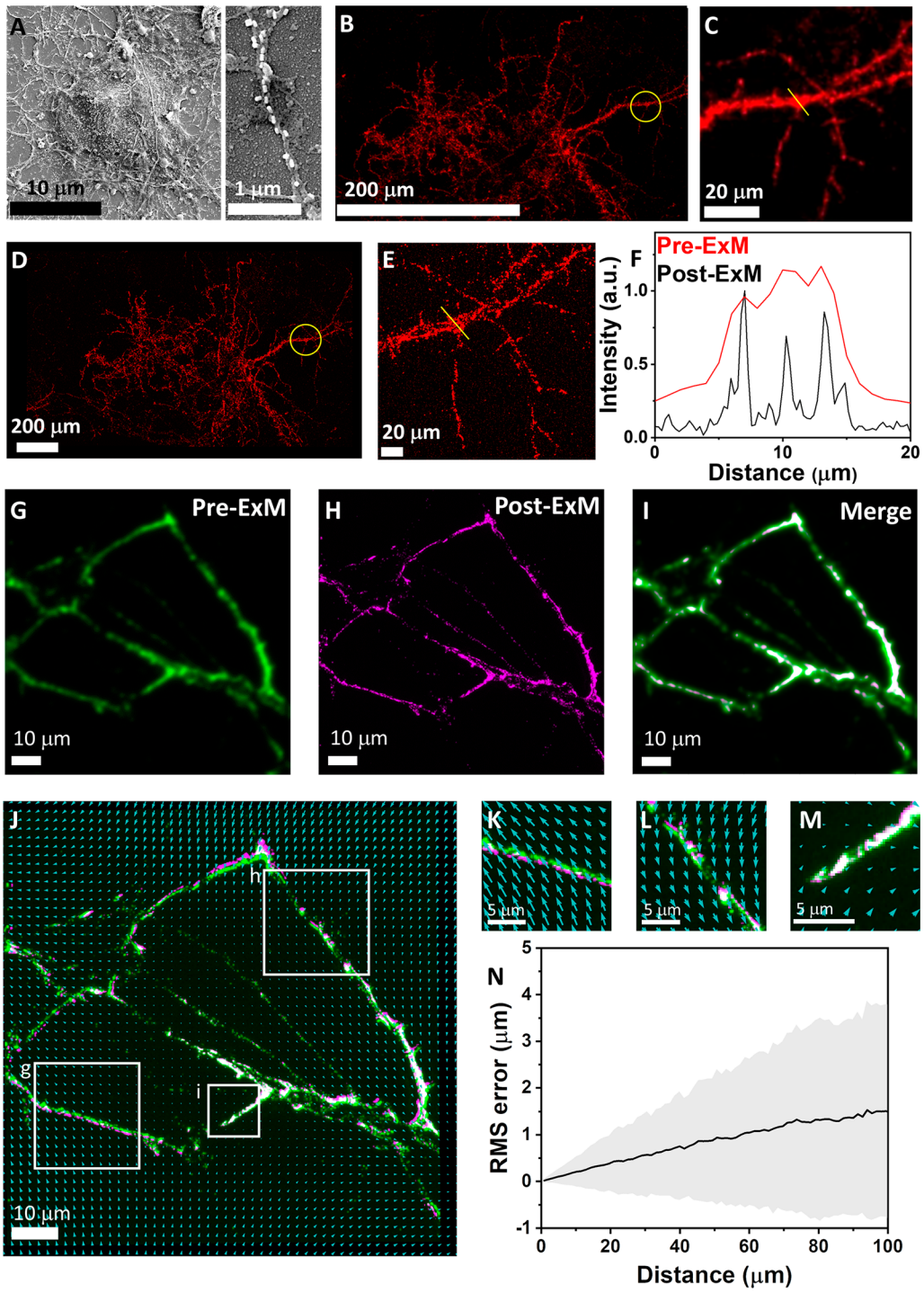

Figure 3. Improved spatial resolution and fidelity of p-ExM. (A) SEM image depicting PFs decorating hippocampal neurons in a random orientation on the soma (left) and longitudinal alignment along the neurites (right). Confocal fluorescence image of cultured hippocampal neurons after 1 h incubation with negatively charged PF-650 (red) (B) pre-ExM, (C) enlarged image of pre-ExM, (D) post-ExM, (E) enlarged image of post-ExM corresponding to the highlighted regions in (B) and (C), respectively. (F) Fluorescence intensity profile along the marked PF-labeled neurite region in pre-ExM and post-ExM imaging. Enlarged confocal microscopy image of PF-labeled hippocampal neurons under (G) pre-ExM conditions interpolated to achieve the same scale as (H) post-ExM. (I) Image showing similarity transformed and b-spline nonrigid registered post-ExM overlay on pre-ExM (a good registration is marked by high-intensity regions). (J) Overlay of post-ExM before and after b-spline nonrigid registration with the vector distortion analysis showing a vector array indicative of transformation required for optimum fitting. (K–M) Enlarged images of arbitrarily identified boxed regions in (J) to study distortions. (N) RMS error measurement as a function of length measurement for post-ExM vs pre-ExM in PF-labeled hippocampal neurons.

detailed information about their structure and distribution. ExM has also been employed to better understand the branching and connectivity within neural networks, the morphology of individual synapses, and the distribution and organization of synaptic proteins. As such, we set out to demonstrate plasmon-enhanced ExM using PF-labeled hippo-

https://doi.org/10.1021/acs.nanolett.3c01256
Nano Lett. 2023, 23, 5654−5662

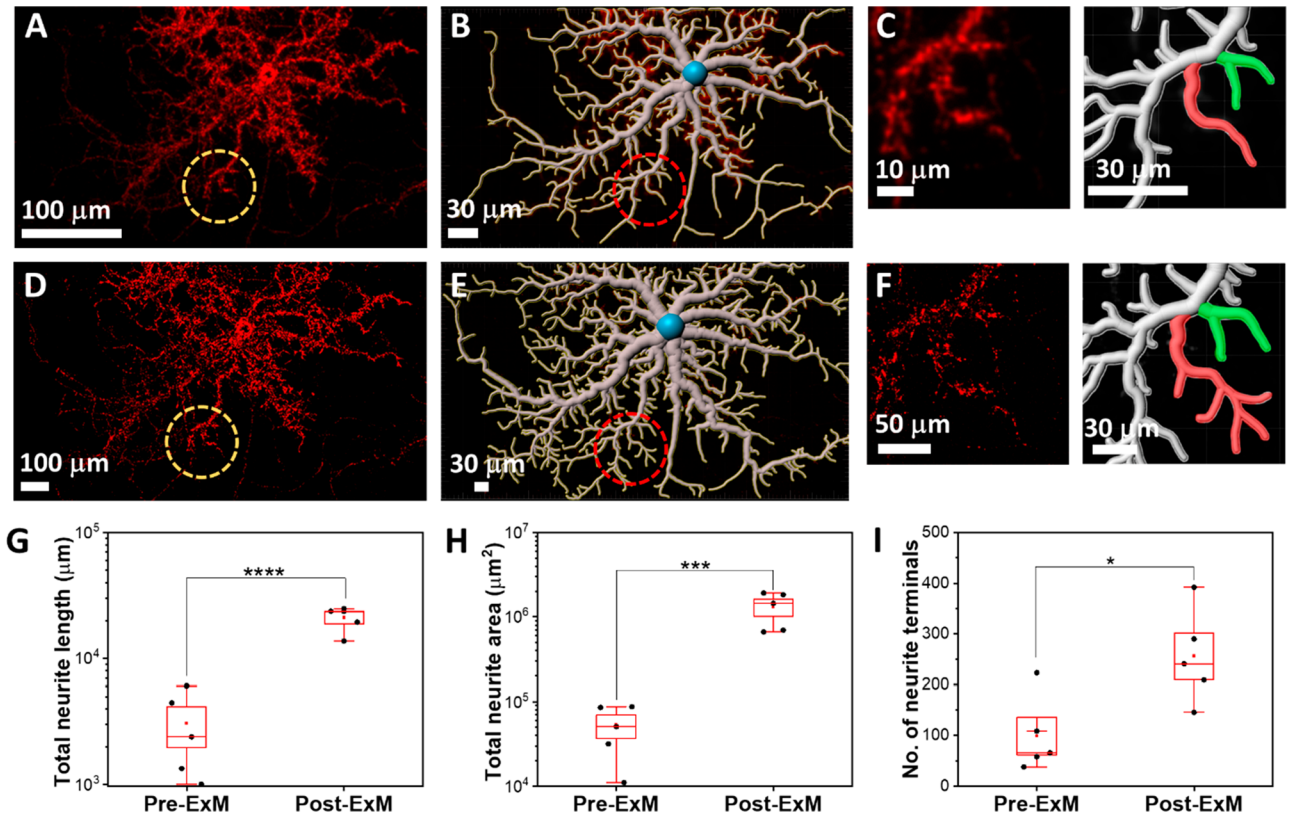

Figure 4. Quantification of neuronal morphological features using p-ExM. Confocal fluorescence image of PF-labeled hippocampal neurons at days in vitro (DIV) 23 under (A) pre-ExM and (D) post-ExM conditions. Corresponding filament traced images generated via a filament tracer module in IMARIS software (Oxford Instruments) for the PF channel under (B) pre-ExM and (E) post-ExM conditions. (C) Enlarged image of highlighted region under pre-ExM conditions (left panel from (A) and right panel from (B); raw vs filament traced plots of spatially identical regions). (F) Enlarged image of highlighted region under post-ExM conditions (left panel from (D) and right panel from (E). The green highlighted filament marks the similarly identified region whereas the red highlighted filament has an 80% higher number of neurite terminals being identified in (F) post-ExM when compared to (C) pre-ExM conditions. Whisker plot representing the morphological maturation parameters (G) total neurite length, (H) total neurite area, and (I) number of neurite terminal points in DIV 23 neurons under pre-ExM and post-ExM conditions, obtained from a filament tracking analysis. Unpaired two-sample *t* test, $n = 5$ PF-labeled neuronal cells from DIV 23, $^{*}p < 0.05$, $^{**}p < 0.01$, $^{***}p < 0.001$, and $^{****}p < 0.0001$.

campal neurons wherein PFs specifically and spontaneously bind to neurons in a maturation-dependent manner (Figure 3 and Figure S1).[24,25] SEM imaging revealed random orientations of PFs on the soma and higher alignment along the length of neurites (Figure 3A).[24] As expected, we observed a bright fluorescence signal from PFs adsorbed on the neuronal cell body and neurites with minimal background, indicating the specific binding of PFs to neurons (Figure 3B). Following the ExM procedure, confocal microscopy images revealed excellent retention of the structural details across a large sample size (~400 × 200 μm^2 in pre-ExM scale) (Figure 3C,E). We observed a remarkable correlation of PF-labeled neurons under post-ExM with pre-ExM conditions over dimensions of 5300 × 2500 μm^2 (Figure S2). Owing to the high density of PFs along the neurites, enlarged images of the neurites in the pre-ExM state showed a diffuse and continuous fluorescence signal along the neurites (Figure 3D). On the other hand, enlarging into the same region of interest in the post-ExM image revealed highly resolved individual PFs (Figure 3E). In contrast to the pre-ExM image, the cross-sectional profile across the neurites obtained from the post-ExM image exhibited three distinct fluorescence signal peaks, highlighting an improvement in resolution and the ability to read a digitized signal via plasmon-enhanced expansion microscopy (Figure 3E,F).

Next, we set out to determine the fidelity of p-ExM images by performing a registration and distortion analysis, which provides quantitative correlation between pre-ExM and post-ExM images. We identified an arbitrary region spanning~100 × 100 μm^2 in pre-ExM and post-ExM images of PF-labeled neurons (Figure 3G,H and Figure S3). Using Elastix, we first performed a similarity transformation on post-ExM image to be matched and aligned to pre-ExM through iterations of isotropic scaling, rotation, and translation along the *x* and *y* directions (Figure S4).[15] By incorporating the scaling factor derived from similarity registration in Elastix, we determined the corrected expansion factor (physical magnification factor) to be 4.0 ± 0.2*X* ($n = 4$), which closely matches with the established protocols.[13,14] Next, we performed a nonrigid b-spline transformation to further correct local deformations in the similarity-transformed post-ExM for better alignment with the pre-ExM conditions (Figure 3I). Subsequently, we plotted the distortion vector field between pre-ExM and post-ExM (Figure 3J−M). We noted an excellent overlap between pre-ExM and transformed post-ExM images, highlighting the need for a minimal deformation correction (Figure S5). The RMS error quantification revealed distortions of ~1.5 μm over length scales of up to ~100 μm, corresponding to ~1.5% error (Figure 3N).

https://doi.org/10.1021/acs.nanolett.3c01256
Nano Lett. 2023, 23, 5654−5662

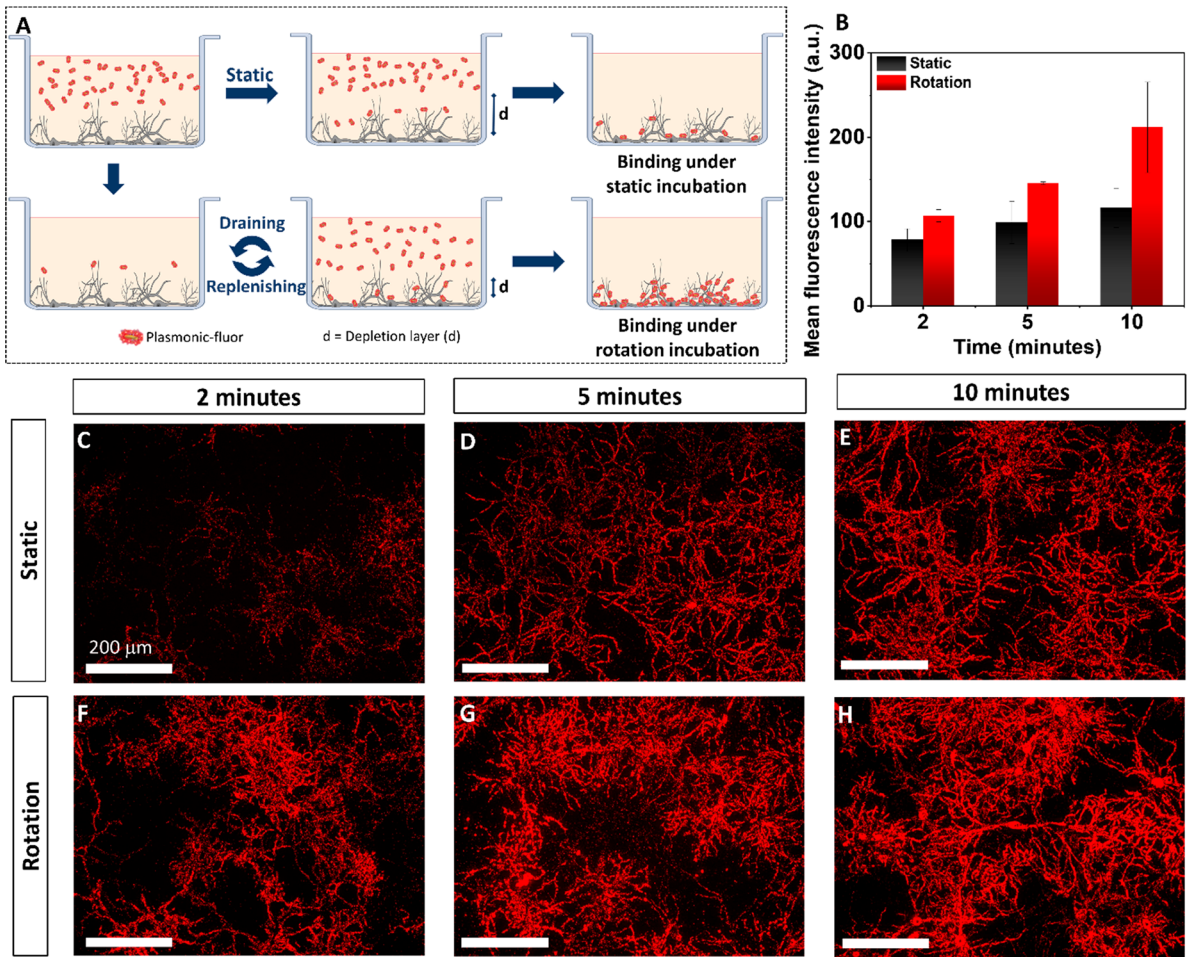

Figure 5. Improving PF-binding kinetics. (A) Schematic depicting the effect of static vs rotational incubation on the labeling efficiency of PFs in neurons. Repeat cycles of draining and replenishing bulky nanolabels facilitates a reduction in the depletion layer and overcoming diffusion limitations. (B) Ensemble mean fluorescence intensity corresponding to static and rotational incubation in DIV 25 neurons (cell density ~20000) (n = 2). Confocal microscopy images (PF-channel) of PF-labeled neurons on DIV 25 under static incubation for (C) 2 min, (D) 5 min, and (E) 10 min. Confocal microscopy images (PF-channel) of PF-labeled neurons on DIV 25 under rotational incubation for (F) 2 min, (G) 5 min, and (H) 10 min.

As demonstrated above, PFs are highly compatible with ExM and exhibit excellent fluorescence retention, and p-ExM offers a significant improvement in the spatial resolution compared to conventional confocal fluorescence microscopy. Building on these results, we set out to harness the improved spatial resolution of p-ExM to identify the previously unresolved fine structure of neurons and the neural network. Toward this end, we employed the filament tracer module in IMARIS software (Oxford Instruments) to quantify the morphological parameters of the neurons. We performed a filament tracking analysis on pre-ExM and post-ExM images of the same set of PF-labeled neurons (n = 5) (Figure 4A,D). Filament tracking revealed a higher density of filaments in the post-ExM image compared to the pre-ExM image (Figure 4B,E). Enlarged images revealed the improved spatial resolution offered by ExM, which enabled improved delineation of the fine neuronal features and analysis of the morphological parameters (Figure 4C,F). We observed a significant increase in the total neurite length, total neurite area, and number of neurite terminals under the post-ExM conditions, indicative of the higher density of filaments being tracked and recognized (Figure 4G–I). A 4-fold expansion of the sample led to a nearly 1.7-fold increase in total neurite length and a nearly 6-fold increase in total neurite area under post-ExM conditions. We observed an ~2.5-fold increase in the number of neurite terminal points under post-ExM conditions owing to enhanced resolution. As opposed to ExM with conventional fluorophores that suffers from severe signal dilution, the fluorescence signal of individual plasmonic-fluors remains undiluted, thus enabling improved quantification of the morphological parameters. These results highlight the efficacy of p-ExM in tracing and mapping the structure of neurons and neuronal networks.

One of the important limitations in using bulky nanoparticles as labels is their slower diffusion compared to conventional molecular fluorophores, which prevents efficient labeling (Figure 5A)[27,28,29]. The characteristic diffusion coefficient (D) relates inversely with the nanolabel size; therefore, the use of bulky nanolabels leads to slower diffusion and the formation of a depletion zone immediately above the surface, with consequently poor binding kinetics on the surface.[30] Therefore, on-surface bioassays and immunohistochemistry labeling often require significantly longer incubation times. To address diffusion limitations associated with the bulky nature of PFs and improve the labeling efficiency of PFs in a neuron cell culture, we adapted a recently introduced cyclic draining and replenishment (CDR) method (Figure 5A

https://doi.org/10.1021/acs.nanolett.3c01256
Nano Lett. 2023, 23, 5654−5662

and Figure S6).[31] Briefly, the substrate with the neuronal network is rotated during the PF labeling step, resulting in cyclical draining and replenishing of the PFs at the surface. After each CDR cycle, the concentration of the PFs at the neuronal surface is replenished to the bulk concentration of nanolabels, thus overcoming the depletion zone and accelerating the labeling process. We exposed the neural culture to PFs for different durations (2, 5, and 10 min) under static and rotation conditions. The ensemble fluorescence intensity was observed to increase by ∼37% for 2 min, ∼44% for 5 min, and ∼83% for 10 min of rotational incubation when compared with static conditions (Figure 5B). With an increase in the incubation time, we observed a rapid increase in the fluorescence from PF-labeled neurons under the rotation conditions (Figure 5C−H).

In conclusion, we introduced plasmon-enhanced expansion microscopy by harnessing recently introduced PFs as nanolabels in expansion microscopy. Plasmonic-fluors, which are nearly 15000-fold brighter compared to corresponding conventional fluorophores, exhibited excellent compatibility with the expansion microscopy protocol. In contrast to most conventional molecular fluorophores, PFs retained nearly 85% of the fluorescence signal after gelation and swelling steps of ExM. We demonstrated that individual PFs can be easily imaged using conventional epifluorescence microscopes and are not prone to signal dilution, making them attractive digital nanolabels in ExM. Harnessing the selective binding of the negatively charged PFs to hippocampal neurons, we demonstrated the high fidelity of p-ExM over large areas of the sample. p-ExM enabled a better visualization and analysis of the morphological features of the neural network, as evidenced by the nearly 2.5-fold increase in the number of neurite terminal points identified by the filament tracking analysis. We also proposed CDR as a method to expedite labeling using nanoparticles, thereby overcoming a key limitation in using such PFs as labeling agents in ExM. In addition to the passive labeling of the neurons, antibody-conjugated PFs can serve as powerful nanolabels for imaging and analyzing low-abundance and sparsely dispersed cell surface markers, which cannot be imaged using conventional molecular fluorophores due to their weak fluorescence signal. The high fidelity of p-ExM and remarkable uniformity of sample expansion make this methodology attractive for probing the structure of neurons and neural networks.

■ ASSOCIATED CONTENT

Supporting Information

The Supporting Information is available free of charge at https://pubs.acs.org/doi/10.1021/acs.nanolett.3c01256.

Description of materials used, methods, experimental procedures, additional confocal fluorescence images (before and after expansion process) of a neural network labeled with plasmonic-fluors, additional fluorescence images used for quantifying the fidelity of the p-ExM process, and phase contrast images of neurons labeled under static and rotation conditions (PDF)

■ AUTHOR INFORMATION

Corresponding Authors

Baranidharan Raman − *Department of Biomedical Engineering, Washington University in St. Louis, St. Louis, Missouri 63130, United States*; Email: barani@wustl.edu

Srikanth Singamaneni − *Department of Mechanical Engineering and Materials Science, and Institute of Materials Science and Engineering, Washington University in St. Louis, St. Louis, Missouri 63130, United States*; orcid.org/0000-0002-7203-2613; Email: singamaneni@wustl.edu

Authors

Priya Rathi − *Department of Chemistry, Washington University in St. Louis, St. Louis, Missouri 63130, United States*

Prashant Gupta − *Department of Mechanical Engineering and Materials Science, and Institute of Materials Science and Engineering, Washington University in St. Louis, St. Louis, Missouri 63130, United States*

Avishek Debnath − *Department of Mechanical Engineering and Materials Science, and Institute of Materials Science and Engineering, Washington University in St. Louis, St. Louis, Missouri 63130, United States*

Harsh Baldi − *Department of Mechanical Engineering and Materials Science, and Institute of Materials Science and Engineering, Washington University in St. Louis, St. Louis, Missouri 63130, United States*

Yixuan Wang − *Department of Mechanical Engineering and Materials Science, and Institute of Materials Science and Engineering, Washington University in St. Louis, St. Louis, Missouri 63130, United States*

Rohit Gupta − *Department of Mechanical Engineering and Materials Science, and Institute of Materials Science and Engineering, Washington University in St. Louis, St. Louis, Missouri 63130, United States*

Complete contact information is available at: https://pubs.acs.org/10.1021/acs.nanolett.3c01256

Notes

The authors declare the following competing financial interest(s): S.S. is one of the inventors on a pending patent related to plasmonic-fluor technology, and the technology has been licensed by the Office of Technology Management at Washington University in St. Louis to Auragent Bioscience LLC. S.S. is one of the co-founders and shareholders of Auragent Bioscience LLC. These potential conflicts of interest have been disclosed and are being managed by Washington University in St. Louis.

■ ACKNOWLEDGMENTS

The authors acknowledge support from the Air Force Office of Scientific Research (FA95501910394) and the National Science Foundation (CBET-1900277 and CBET-2224610). The authors thank the Institute of Materials Science and Engineering at Washington University for providing access to electron microscopy facilities. The authors thank Dr. Aaron Halpern for helping with Elastix analysis.

■ REFERENCES

(1) Hell, S. W. Far-Field Optical Nanoscopy. *Science* **2007**, *316*, 1153.

(2) Westphal, V.; Hell, S. W. Nanoscale resolution in the focal plane of an optical microscope. *Phys. Rev. Lett.* **2005**, *94* (14), 143903.

(3) Alberts, B. *Molecular biology of the cell*, 4th ed.; Garland Science: 2002.

(4) Hell, S. W.; Wichman, J. Breaking the diffraction resolution limit by stimulated emission:stimulated-emission-depletion fluorescence microscopy. *Opt. Lett.* **1994**, *19* (11), 780.

(5) Neil, M. A. A.; Juskaitis, R.; Wilson, T. Method of obtaining optical sectioning by using structured light in a conventional microscope. *Opt. Lett.* **1997**, *22* (24), 1905.
(6) Sigal, Y. M.; Zhou, R.; Zhuang, X. Visualizing and discovering cellular structures with super-resolution microscopy. *Science* **2018**, *361* (6405), 880−887.
(7) Blom, H.; Widengren, J. Stimulated Emission Depletion Microscopy. *Chem. Rev.* **2017**, *117* (11), 7377−7427.
(8) Rust, M. J.; Bates, M.; Zhuang, X. Sub-diffraction-limit imaging by stochastic optical reconstruction microscopy (STORM). *Nat. Methods* **2006**, *3* (10), 793−5.
(9) Huang, B.; Wang, W.; Bates, M.; Zhuang, X. Three-Dimensional Super-Resolution Imaging by Stochastic Optical Reconstruction Microscopy. *Science* **2008**, *319*, 810.
(10) Balzarotti, F.; Eilers, Y.; Gwosch, K. C.; Gynna, A. H.; Westphal, V.; Stefani, F. D.; Elf, J.; Hell, S. W. Nanometer resolution imaging and tracking of fluorescent molecules with minimal photon fluxes. *Science* **2017**, *355*, 606.
(11) Schmidt, R.; Weihs, T.; Wurm, C. A.; Jansen, I.; Rehman, J.; Sahl, S. J.; Hell, S. W. MINFLUX nanometer-scale 3D imaging and microsecond-range tracking on a common fluorescence microscope. *Nat. Commun.* **2021**, *12* (1), 1478.
(12) Mockl, L.; Moerner, W. E. Super-resolution Microscopy with Single Molecules in Biology and Beyond-Essentials, Current Trends, and Future Challenges. *J. Am. Chem. Soc.* **2020**, *142* (42), 17828−17844.
(13) Chen, F.; Tillberg, P. W.; Boyden, E. S. Expansion Microscopy. *Science* **2015**, *347* (6221), 543.
(14) Tillberg, P. W.; Chen, F.; Piatkevich, K. D.; Zhao, Y.; Yu, C. C.; English, B. P.; Gao, L.; Martorell, A.; Suk, H. J.; Yoshida, F.; DeGennaro, E. M.; Roossien, D. H.; Gong, G.; Seneviratne, U.; Tannenbaum, S. R.; Desimone, R.; Cai, D.; Boyden, E. S. Protein-retention expansion microscopy of cells and tissues labeled using standard fluorescent proteins and antibodies. *Nat. Biotechnol.* **2016**, *34* (9), 987−92.
(15) Chozinski, T. J.; Halpern, A. R.; Okawa, H.; Kim, H. J.; Tremel, G. J.; Wong, R. O.; Vaughan, J. C. Expansion microscopy with conventional antibodies and fluorescent proteins. *Nat. Methods* **2016**, *13* (6), 485−8.
(16) Trinks, N.; Reinhard, S.; Drobny, M.; Heilig, L.; Loffler, J.; Sauer, M.; Terpitz, U. Subdiffraction-resolution fluorescence imaging of immunological synapse formation between NK cells and A. fumigatus by expansion microscopy. *Commun. Biol.* **2021**, *4* (1), 1151.
(17) Liu, J.; Fang, X.; Liu, Z.; Li, R.; Yang, Y.; Sun, Y.; Zhao, Z.; Wu, C. Expansion Microscopy with Multifunctional Polymer Dots. *Adv. Mater.* **2021**, *33* (25), 2007854.
(18) Min, K.; Cho, I.; Choi, M.; Chang, J. B. Multiplexed expansion microscopy of the brain through fluorophore screening. *Methods* **2020**, *174*, 3−10.
(19) Cho, I.; Sim, J.; Chang, J. B. Expansion microscopy imaging of various neuronal structures. *Methods Cell Biol.* **2021**, *161*, 83−103.
(20) Luan, J.; Seth, A.; Gupta, R.; Wang, Z.; Rathi, P.; Cao, S.; Gholami Derami, H.; Tang, R.; Xu, B.; Achilefu, S.; Morrissey, J. J.; Singamaneni, S. Ultrabright fluorescent nanoscale labels for the femtomolar detection of analytes with standard bioassays. *Nat. Biomed Eng.* **2020**, *4* (5), 518−530.
(21) Seth, A.; Mittal, E.; Luan, J.; Kolla, S.; Mazer, M. B.; Joshi, H.; Gupta, R.; Rathi, P.; Wang, Z.; Morrissey, J. J.; Ernst, J. D.; Portal-Celhay, C.; Morley, S. C.; Philips, J. A.; Singamaneni, S. High-resolution imaging of protein secretion at the single-cell level using plasmon-enhanced FluoroDOT assay. *Cell Rep. Methods* **2022**, *2* (8), 100267.
(22) Wang, Z.; Luan, J.; Seth, A.; Liu, L.; You, M.; Gupta, P.; Rathi, P.; Wang, Y.; Cao, S.; Jiang, Q.; Zhang, X.; Gupta, R.; Zhou, Q.; Morrissey, J. J.; Scheller, E. L.; Rudra, J. S.; Singamaneni, S. Microneedle patch for the ultrasensitive quantification of protein biomarkers in interstitial fluid. *Nat. Biomed Eng.* **2021**, *5* (1), 64−76.
(23) Wang, Z.; Zhou, Q.; Seth, A.; Kolla, S.; Luan, J.; Jiang, Q.; Rathi, P.; Gupta, P.; Morrissey, J. J.; Naik, R. R.; Singamaneni, S. Plasmonically-enhanced competitive assay for ultrasensitive and multiplexed detection of small molecules. *Biosens Bioelectron* **2022**, *200*, 113918.
(24) Gupta, P.; Rathi, P.; Gupta, R.; Baldi, H.; Coquerel, Q.; Debnath, A.; Derami, H. G.; Raman, B.; Singamaneni, S., Neuronal Maturation-dependent Nano-Neuro Interaction and Modulation. *bioRxiv* 2022, 2022.08.03.502650.
(25) Dante, S.; Petrelli, A.; Petrini, E. M.; Marotta, R.; Maccione, A.; Alabastri, A.; Quarta, A.; De Donato, F.; Ravasenga, T.; Sathya, A.; Cingolani, R.; Proietti Zaccaria, R.; Berdondini, L.; Barberis, A.; Pellegrino, T. Selective Targeting of Neurons with Inorganic Nanoparticles: Revealing the Crucial Role of Nanoparticle Surface Charge. *ACS Nano* **2017**, *11* (7), 6630−6640.
(26) Ku, T.; Swaney, J.; Park, J.-Y.; Albanese, A.; Murray, E.; Cho, J. H.; Park, Y.-G.; Mangena, V.; Chen, J.; Chung, K. Multiplexed and scalable super-resolution imaging of three-dimensional protein localization in size-adjustable tissues. *Nat. Biotechnol.* **2016**, *34* (9), 973−981.
(27) Pereiro, I.; Fomitcheva-Khartchenko, A.; Kaigala, G. V. Shake It or Shrink It: Mass Transport and Kinetics in Surface Bioassays Using Agitation and Microfluidics. *Anal. Chem.* **2020**, *92* (15), 10187−10195.
(28) Sotnikov, D. V.; Zherdev, A. V.; Dzantiev, B. B. Mathematical Modeling of Bioassays. *Biochemistry (Mosc)* **2017**, *82* (13), 1744−1766.
(29) Stenberg, M.; Nygren, H. Kinetics of antigen-antibody reactions at solid-liquid interfaces. *Journal of Immunological Methods* **1988**, *113* (113), 3.
(30) Wang, G.; Driskell, J. D.; Porter, M. D.; Lipert, R. J. Control of Antigen Mass Transport via Capture Substrate Rotation: Binding Kinetics and Implications on Immunoassay Speed and Detection Limits. *Anal. Chem.* **2009**, *81* (15), 6175.
(31) Li, J.; Zrazhevskiy, P.; Gao, X. Eliminating Size-Associated Diffusion Constraints for Rapid On-Surface Bioassays with Nanoparticle Probes. *Small* **2016**, *12* (8), 1035−1043.

https://doi.org/10.1021/acs.nanolett.3c01256
Nano Lett. 2023, 23, 5654−5662